Materials Advances

ROYAL SOCIETY OF CHEMISTRY

PAPER

View Article Online
View Journal | View Issue

Cite this: *Mater. Adv.*, 2022, 3, 8780

Synthesis and ionic conductivity of calcium-doped ceria relevant to solid oxide fuel cell applications†

Naeemakhtar Momin,[a] J. Manjanna,*[a] Satoru Kobayashi,[b] S. T. Aruna,[c] S. Senthil Kumar[c] and G. P. Nayaka[d]

Received 16th August 2022,
Accepted 2nd October 2022

DOI: 10.1039/d2ma00868h

rsc.li/materials-advances

Towards the development of green energy devices, it is necessary to focus on commercial electrolyte materials for intermediate temperature solid oxide fuel cells (IT-SOFCs). Ca-doped ceria (CDC) samples having a composition of $Ce_{(1-x)}Ca_xO_{2-\delta}$ ($0.03 \leq x \leq 0.1$) were synthesized by a facile solid-state route and sintered at a lower temperature (1473 K). X-ray diffraction, Raman, X-ray photoelectron, Fourier-transform infrared, UV–VIS diffuse reflectance, field emission scanning electron microscopy – energy dispersive X-ray with elemental mapping, and electrochemical impedance spectroscopy techniques were used for the characterization of these CDC samples. The 0.10 CDC showed high oxide ion conductivity of 8.01×10^{-3} S cm^{-1} at 973 K with a lower activation energy of 0.78 eV. The 0.03 CDC, 0.05 CDC, and 0.07 CDC samples exhibited ionic conductivities of 1.66×10^{-4}, 4.42×10^{-3}, and 5.76×10^{-3} S cm^{-1} at 973 K with activation energies of 1.65, 1.01, and 0.92 eV, respectively. The present work aims to develop Ca-doped ceria as economically viable electrolytes for IT-SOFCs.

Introduction

Solid oxide fuel cells (SOFCs) are known to convey high electrical proficiency and fuel adaptability with ensured natural advantages. In SOFCs, the hopping mechanism regulates the ions through electrolytes between the cathode and anode. The high ionic and insignificant electronic conductivity, permanence in redox conditions, mechanical strength (among other qualities) are viewed as great properties for electrolyte materials. An assortment of oxide-ion electrolytes have been examined up to this point, similar to zirconia-based oxides, cubic fluorite structure based doped ceria, stabilized δ-Bi_2O_3 and others. The issues related to their cost, electronic conduction, working and sintering temperature discourage its mass scale commercialization.[1] The doped ceria-based ceramics were found to show almost the same results at intermediate temperature (IT), 773–973 K for SOFC applications. The conduction mechanism in doped ceria was influenced by the mobility and distribution of oxygen vacancies. It is created by substituting suitable cations with lower valences than the host lattice ions. The rare earth-doped ceria-based materials have been examined because of their ability to yield high ionic conductivity at lower temperatures and are thus viewed as a prospective electrolyte for IT-SOFCs.[2,3] The Sm and Gd ionic radii coordinate well with Ce ions, and hence high oxide-ion conductivity has been accounted for GDC10 and SDC20. The Gd-, Sm-, and Y-doped ceria having a high dopant concentration of 15–20 mol%, showed improved ionic conductivity at elevated temperatures.[4,5] In any case, the ideal ionic conductivity at lower temperatures actually has not been accomplished, and subsequently, their expense for 10–20 mol% dopant amount is not economically reasonable.[6] Thus, there exists an expansive degree in the advancement of new economically reasonable ceria-based electrolyte materials. The alkaline earth-doped ceria materials have been viewed as substantially more powerful and potential candidate to yield huge ionic conductivity at lower temperatures. For example, Ce (r_i = 1.11 Å) doped with Ca (r_i = 1.12 Å) has been researched among the alkaline earth-doped ceria-based materials. The ionic conductivities of alkaline earth-doped ceria-based materials are viewed as critically as those of rare earth-doped materials. A high conductivity on the order of 10^{-3} S cm^{-1} was reported by Yamashita *et al.*[7] at 873 K for the $Ce_{0.9}Ca_{0.1}O_{2-\delta}$ composition. Similarly, Banerjee *et al.*[8] reported 1.29×10^{-2} S cm^{-1} for oxide ion conductivity at 873 K for the $Ce_{0.8}Ca_{0.2}O_{2-\delta}$ composition prepared through the auto-combustion method. Calcium is abundant in nature and cheaper than other rare earth elements,[9] and its doping is found to create higher oxygen vacancies. Therefore, it has been

[a] *Department of Chemistry, Rani Channamma University, Belagavi-591156, Karnataka, India. E-mail: jmanjanna@rediffmail.com; Tel: +91-9916584954*
[b] *Department of Material Science and Engineering, Iwate University, Morioka-020-8551, Japan*
[c] *Surface Engineering Div., CSIR-National Aerospace Laboratories, Bengaluru-560017, Karnataka, India*
[d] *Physical & Materials Chemistry Div., CSIR-National Chemical Laboratory, Pune 411008, Maharashtra, India*

† Electronic supplementary information (ESI) available. See DOI: https://doi.org/10.1039/d2ma00868h

regarded as an excellent and advanced oxygen storage material.[10] Subsequently, for economical reasonability, cheap dopants such as Ca having sufficient electrochemical performance have been considered favorable. Recently, Schottky junction (SJ)-based n or p-type low-cost semiconductor – ionic conductor composite materials have shown potential to cause in-filed barriers and confine the electron's mobility or holes from the passage of the electrolyte edge to the opposite side. Thus, this prevents the short-circuiting in the SOFCs and may be accountable for the colossal ionic conductivity.[11–22] Still, there are few studies related to the Ca-doped ceria framework for IT-SOFCs. From the point of the ionic-radius, compatibility of the dopant, commercial viability, and abundant nature, calcium (Ca) has been picked as a dopant for the host cerium cross-section. In the present work, the CDC samples were prepared by the conventional solid-state method, and calcium has likewise been viewed as a sintering aid for the ceria-based electrolytes.[23] Sintering ceria-based electrolytes above 1573 K prompts the reduction of some Ce^{4+} to Ce^{3+} ions, causing electronic leakage and affecting the performance of the cell.[24] Therefore, attempts have been made to achieve the high densification at a lower sintering temperature of 1473 K than the required high-temperature sintering in the range of 1873–1973 K (Yamashita *et al.* 1995).[8] The oxide ion conductivities of CDC samples are studied as a function of dopant concentrations between the temperature range of 623–973 K in air using electrochemical impedance spectroscopy. This work accordingly plans to investigate the new low-cost Ca-doped ceria ceramics for IT-SOFCs.[25]

Experimental

The Ca-doped CeO_2 ceramic oxide powders with the composition $Ce_{1-x}Ca_xO_{2-\delta}$ (x = 0.03, 0.05, 0.07 and 0.1) are prepared from conventional solid-state route by using cerium oxide [A.R grade 99.99% pure, Sd-Fine Mumbai-India] and hydrated calcium acetate [$C_4H_6O_4Ca{\cdot}XH_2O$]; [A.R grade 99.99% pure, Sd-Fine Mumbai-India]. The stoichiometric ratios of precursors were blended with isopropyl alcohol manually for 1 h, and calcined at 1273 K for 6 h in a muffle furnace. The obtained powders were again ground and pelletized (10 ϕ × 2 mm dimensions), and sintered at 1473 K in the air for 4 h. The final obtained products having different compositions are hereinafter referred to as 0.03 CDC, 0.05 CDC, 0.07 CDC and 0.10 CDC individually.

Characterization

The XRD analysis of CDC samples was carried out using a Rigaku MiniFlex 600 powder X-ray diffractometer (Cu Kα rad., λ = 1.54 Å) instrument. The Archimedes principle was used to determine the relative densities of the pellets.[26] The DILOR-JOBIN-YVON-SPEX-623 nm was used to record the Raman spectra of the CDC pellets. XPS spectra of the CDC samples were recorded from a Thermo Fisher Scientific Instrument (Al K_α + $h\nu$ = 1486.68 eV, spot size 400 μm). The total reflectance (spectral + diffused) spectra of the CDC samples were recorded using a JASCO spectrophotometer, V-77. The Bruker instrument (Nano GmbH Berlin, Germany) was used to record the FESEM images, EDX spectra and elemental mapping of the CDC samples. The a.c. impedance analysis was carried out in air at 1 atm using a CH Instrument (Inc CHI604D, USA). The CDC pellets were silver painted and baked at 773 K for 1 h for electrical connections. The Nyquist plots were obtained between the temperature ranges of 623–973 K and frequency range of 1–10^6 Hz with an a.c signal of 10 mA. The obtained data were fitted to an equivalent electrical circuit, [R(QR)(QR)] with ZSimpWin software. The conductivity was calculated using eqn (1):

$$\sigma = t/RA \quad (1)$$

with thickness (t), area of cross-section (A), and R is the resistance.[27]

Results and discussion

Fig. 1 illustrates the XRD patterns of the pellet CDC samples. The XRD patterns of the powder CDC samples are shown in Fig. 1S as ESI.† The XRD patterns exhibited the same cubic-fluorite structure as per the space group $Fm\bar{3}m$. The planes of the preferential peaks were indexed as per the ICDD card no. 34-0394. It was observed that no peaks of CaO or other impure phases were detected in all XRD patterns of the powder and pellet CDC samples. The XRD analysis revealed that the samples consist of a characteristic lattice structure that matches the standard CeO_2.[28,29] A trivial expansion in the lattice constant upon doping has been attributed to the substitution of the Ce ion by Ca, which caused strain and a slight deformation of the structure. To hold the charge balance, the initiated oxygen

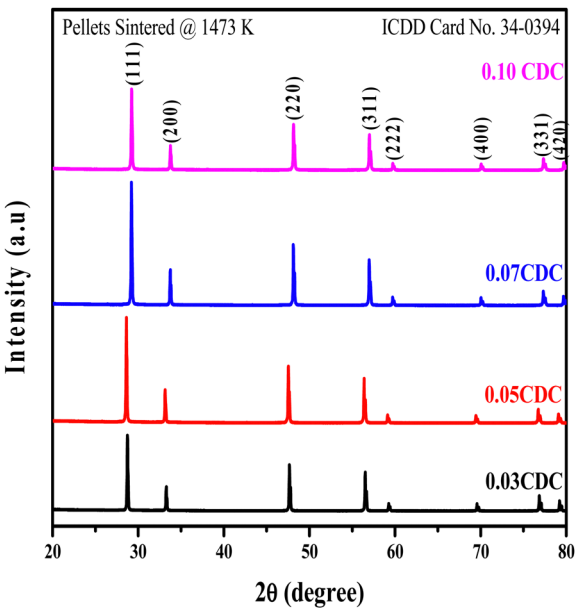

Fig. 1 XRD pattern of CDC pellets sintered at 1473 K.

Table 1 Structural parameters of CDC pellets sintered at 1473 K

Samples	Average crystallite size (D) (nm) Scherrer	Lattice constant ($a = b = c$) (Å)	Volume (Å)^3	Dislocation density (δ) (line per m^2 × 10^{-15})	Specific surface area (m^2 g^{-1})	Bandgap, E_g (eV)	Relative density (%)
0.03 CDC	67.7	5.413	158.6	0.218	0.128	2.98	94.97
0.05 CDC	84.7	5.414	158.6	0.139	0.981	2.88	96.78
0.07 CDC	86.1	5.418	159.1	0.134	0.968	2.82	95.12
0.10 CDC	93.8	5.419	159.3	0.113	0.885	2.80	95.58

vacancies in the cerium lattice will extend the unit cell to limit the strain.[30,31] Likewise, expansion of the lattice constant changes the d-spacing, causing a shift of the diffraction peaks to bring down the 2θ positions. Hence, the lattice parameters of the CDC samples increase with the dopant (Ca) concentration, as shown in Table 1. Furthermore, the high-temperature sintering of the pellets (1473 K) results in sharp peaks of increased intensity with large particle sizes, indicative of the highly crystallinity due to the grain growth.[32,33]

The Scherrer equation was used to determine the crystallite size from the width of the preferential planes. The dislocation density was found to increase with dopant content.

The lower values of dislocation density observed in the CDC pellets are likely due to the excellent crystallinity of the CDC samples.[34] The computed theoretical surface area of the CDC samples appreciably varied with the dopant content and dislocation density.[35] The average crystallite size, dislocation density and specific surface area values are summarized in Table 1. The relative density of the CDC pellets was found to be around 95% and is listed in Table 1. The relative density of the CDC pellets shows an increasing trend with dopant concentrations.

Fig. 2 shows the Raman spectra of the CDC pellets. The presence of a distinct intense peak at 464–461 cm^{-1} has been credited to the F_{2g} Raman active mode of the fluorite structure. This is because of the symmetrical breathing mode of the Ce–O8 vibration unit.[36–38] Furthermore, the Raman active mode F_{2g} shifts to a lower frequency amid a rise in the dopant (Ca) content. The adjustment of the bond length, cross-section dispersion, and nuclear geometry of CeO_2, which is the result of Ce–O bond breaking, emerged because of the generation of oxygen vacancies during the replacement of Ca-ions into the cerium lattice. The produced oxygen vacancies are facilitated with Ce and Ca ions, and decrease to change the length of the Ce–O and Ca–O bonds, and determine the moving of the F_{2g} mode to bring down the frequencies. In Ca-doped CeO_2, the F_{2g} Raman-active mode showed more extensive and asymmetric peaks in contrast to the unadulterated CeO_2. This asymmetric nature and expansion in the FWHM upsides of the F_{2g} mode result from the improved lattice strain after doping, prompting the production of an excessive amount of oxygen vacancies.[39–42] Furthermore, no other peaks are detected for impurities (like CaO), which in corroboration with the XRD study, established the formation of single-phase solid solutions.

The XPS analysis was employed to study the microstructure and chemical state of the CDC samples. Fig. 3(a)–(c) shows the typical XPS spectra of the 0.05 CDC, 0.07 CDC and 0.10 CDC samples sintered at 1473 K. The presence of three different

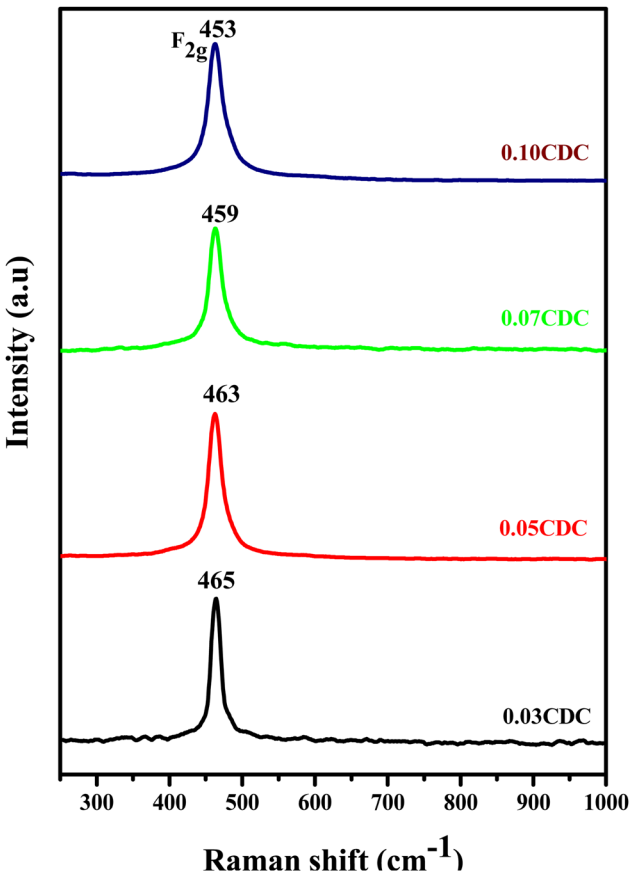

Fig. 2 Raman spectra of the CDC pellets.

sections at around 880–890 eV, 895–910 eV, and at 916 eV of the Ce 3d core-level spectra is evident in all CDC samples.[43] The existence of the Ce^{4+} state consigned to the $4f^0$ orbital transition is designated by the peak at 916 eV.[44] The charge transfer from the oxygen 2p to Ce 4f states could resulted in the three doublets having configurations of 3d $4f^0$, 3d$4f^1$ (L), and 3d $4f^2$ $(L)^2$.[45] The Ce 3d spectra of these samples displayed the six characteristic peaks in the binding energy (BE) range of 870 to 930 eV. The Ce 3d XPS spectrum consists of two spin–orbit splitting of multiplets of $3d_{5/2}$ and $3d_{3/2}$ core holes. The final state of $4f^0$–O $2p^6$ was represented by u‴ and v‴, and corresponds to high binding energy peaks. The u″, v″, u and v represent the $4f^1$–O $2p^5$ and $4f^2$–O $2p^4$ states and correspond to lower binding energy peaks.[46] The binding energy peaks observed for the $3d_{5/2}$ core hole multiplets (0.05 CDC: 883.3, 889, 898), (0.07 CDC: 883.2, 888.8, 898 eV) and (0.10 CDC: 882.4, 887.5, 897 eV) are nearly in the same

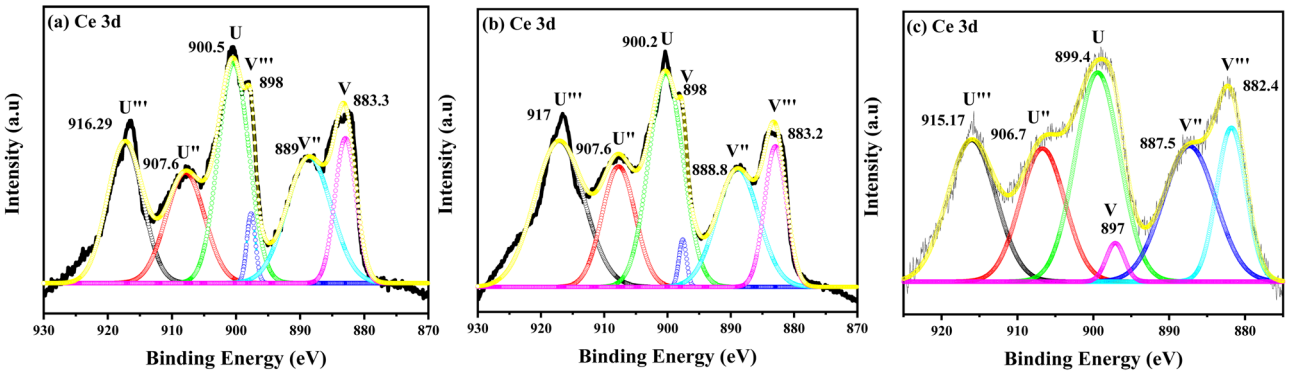

Fig. 3 Ce 3d level experimental and peak fitting XPS spectra of (a) 0.05 CDC, (b) 0.07 CDC, and (c) 0.10 CDC.

range, and a marginal decrease in the binding energy for V′′′ has been observed in all samples. The decreasing trend may be attributed to the increasing content of the dopant. Similarly, the binding energy peaks observed for the $3d_{3/2}$ core hole multiplets (0.05 CDC: 900.5, 907.6, 916.2), (0.07 CDC: 900.2, 907.6, 917 eV) and (0.10 CDC: 899.4, 906.7, 915.17 eV) are in good agreement with those that have been reported. The Ce 3d XPS spectra consist of some indistinguishable overlapped peaks corresponding to both Ce^{4+} and Ce^{3+} states, which make the spectra more complex. Most of the peaks in all of the spectra correspond to the Ce^{4+} state, and the BE peaks at 889, 888.8 and 887.8 eV of $3d_{5/2}$ and 900.5, 900.2 and 899.4 eV of $3d_{3/2}$ appeared for the 0.05 CDC, 0.07 CDC and 0.10 CDC samples, correspond to the Ce^{3+} state respectively.

The XPS spectra of the Ca 2p core-level with deconvolution peaks are shown in Fig. 4(a)–(c) of the CDC samples, and display the $2p_{1/2}$ and $2p_{3/2}$ states, which are split into two final states, I and II. Due to the spin–orbit splitting, these are distinguishable at around 347.2, 347.2 and 347.1 eV, corresponding to the $2p_{3/2}$ state, and 350.3, 350.2 and 352 eV, corresponding to the $2p_{1/2}$ state of the 0.05 CDC, 0.07 CDC and 0.10 CDC samples respectively.[47,48]

Fig. 5(a)–(c) show the O1s XPS spectra deconvoluted into the different symmetrical signals of the CDC samples. The O 1s

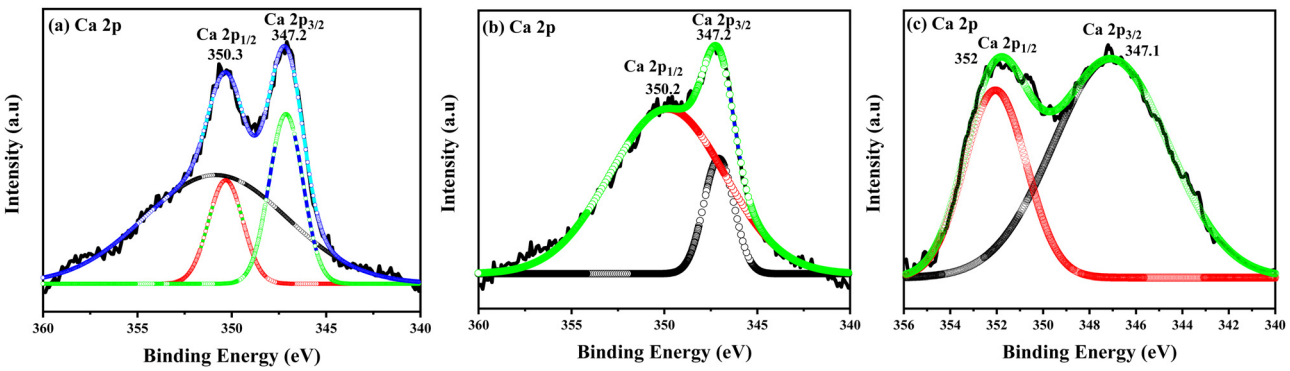

Fig. 4 Ca 2p level experimental and peak fitting XPS spectra of (a) 0.05 CDC, (b) 0.07 CDC, and (c) 0.10 CDC.

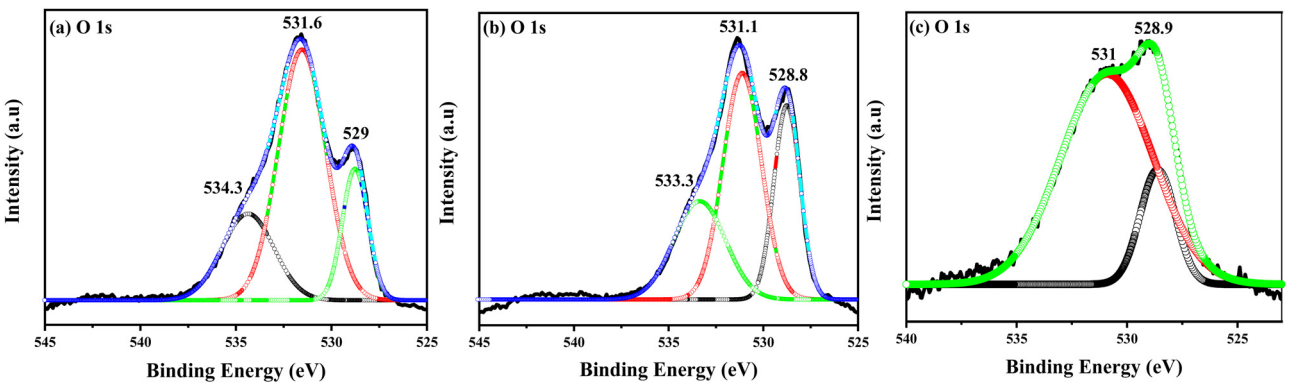

Fig. 5 O 1 s level experimental and peak fitting XPS spectra of (a) 0.05 CDC, (b) 0.07 CDC, and (c) 0.10 CDC.

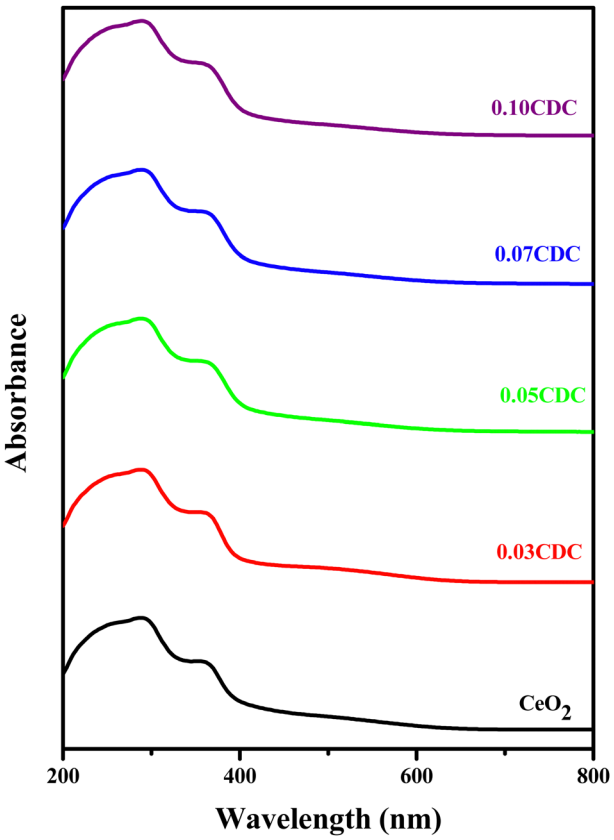

Fig. 6 UV-Visible diffuse reflectance spectra of the CDC samples.

spectra show two different peaks at 528.5, 528.8, and 528.9 eV, and at 531.7, 531.3, and 531 eV for the 0.05, 0.07 and 0.010 CDC, respectively. The sharp intense peaks were attributed to the lattice oxygen of the CDC samples, and the other peaks are assigned to the existence of hydroxyl groups due to exterior contaminations on the sample. The high content of Ca in 0.10 CDC may have shifted the binding energy peak, as observed in Fig. 5(c).[49]

The 1s oxygen spectra were deconvoluted into contributions from the Ca–O, Ce^{3+}–O, and Ce^{4+}–O bound species because the cerium atom in the +3 oxidation state would be more tightly bound than cerium in the +4 state.[50] Upon examining the peaks' relative area, a portion of the CeO_x exists in the Ce^{3+} state.[51] The obtained XPS spectra of the CDC samples show apparent CeO_2 features and the existence of a Ca 2p signal, indicating that the Ca particles have been doped into the CeO_2 lattice. This is corroborated by the XRD and Raman analyses of the CDC samples, and matches well with results reported in the literature.[52]

The diffuse reflectance (DR) UV-visible absorption spectra of the CDC samples are depicted in Fig. 6. The appearance of sharp intense peaks in the ultraviolet absorption region around 290–295 nm is ascribed to the charge transition from the O 2p to Ce 4f, and is assumed to be caused by the oxygen vacancies.[53] This red-shift is attributed to the interfacial polaron effect emerging from the electron–phonon interaction.[54] The Kubelka–Munk plots of the CDC samples for the optical band gap are shown in Fig. 4S (ESI†). The obtained band gap energy values are summarized in Table 1.

The FESEM images of the CDC pellets are shown in Fig. 7. Some particles were seen on the surface. This may be due to the powder, which is used as a bed during the sintering process.

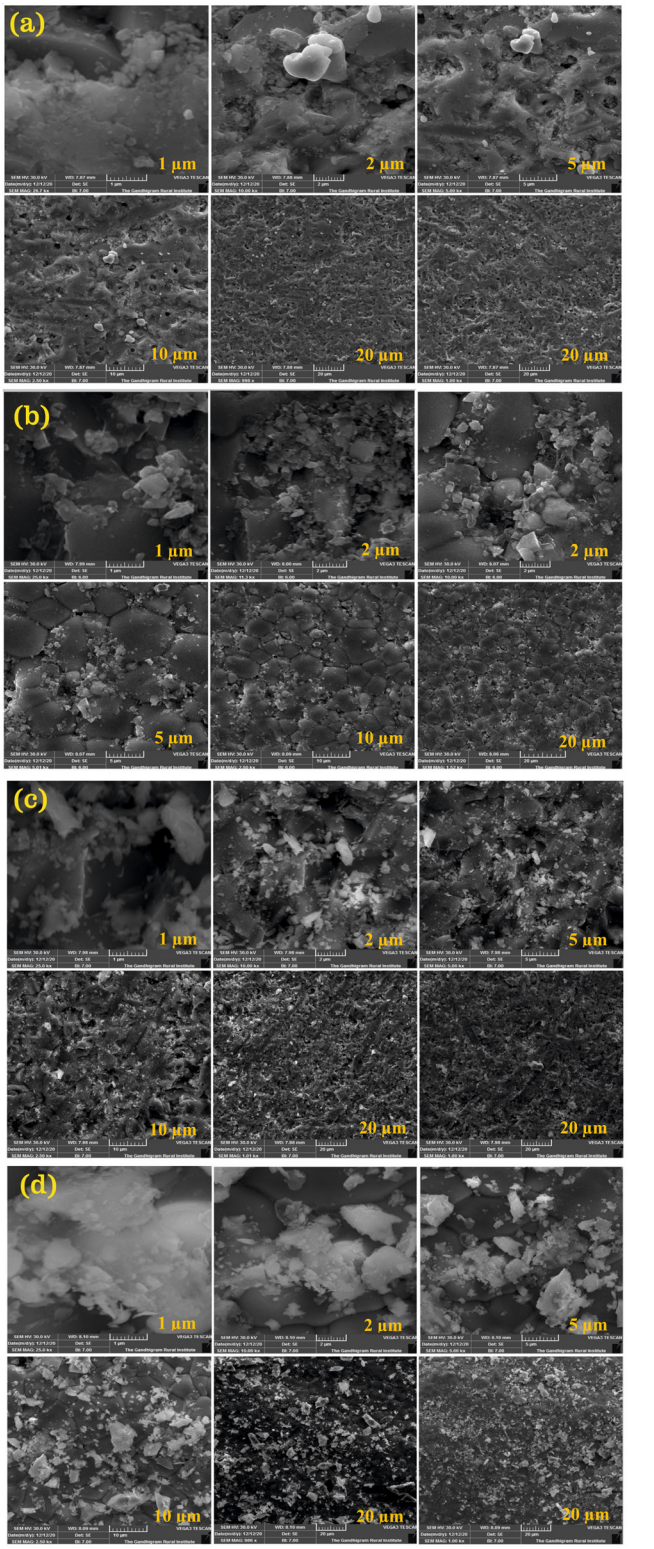

Fig. 7 FE-SEM images of (a) 0.03 CDC, (b) 0.05 CDC, (c) 0.07 CDC, and (d) 0.1 CDC.

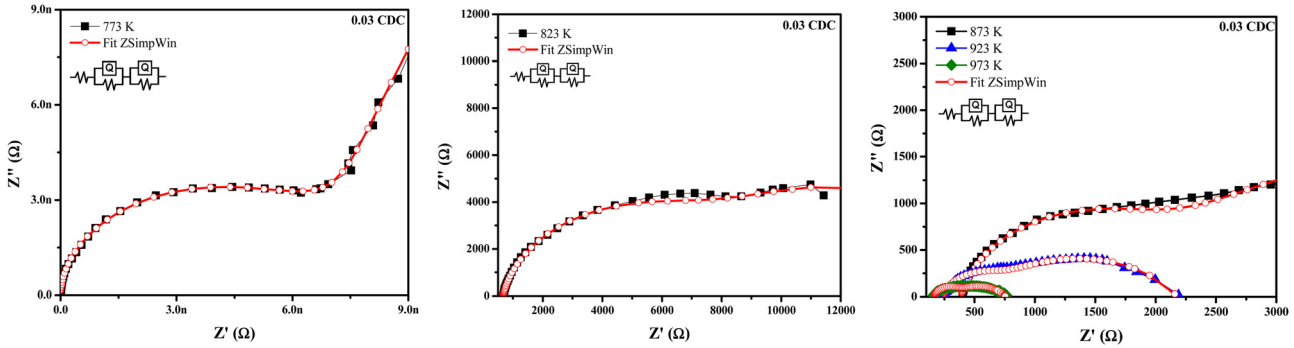

Fig. 8 Nyquist plots of 0.03 CDC measured at temperatures between 773–973 K.

Generally, high-temperature sintering yields a larger particle size.[55] All CDC samples have been observed to be highly dense with the absence of intra-granular pores. Hence, it may be concluded that these samples achieved good densification. The EDX and elemental mapping of the CDC samples are shown in Fig. 5S (ESI†), and it confirmed the existence of Ce, Ca, and O elements. The EDX analysis revealed that the elemental composition of all CDC samples are in good agreement with those with the proposed stoichiometric amounts. The EDX elemental mapping analysis revealed that the amount of dispersion for Ca was low compared to Ce, and confirmed the uniform distribution of elements throughout the matrix.[56]

Fig. 8–11 show the Nyquist plots of the 0.03 CDC, 0.05 CDC, 0.07 CDC, and 0.10 CDC samples, respectively. To distinguish the overlapped grain, grain boundary (GB), and electrode contributions, an equivalent electrical circuit model [R(QR)(QR)] was used, as shown in the inset of Fig. 8. This comparable circuit comprises two RC components in series for the grain resistance (R_g) and GB (R_{gb}), and others for the electrode polarization (R_e). A constant phase element (CPE = Q) is applied rather than a capacitor. This Q is comparable to the dispersion of the capacitor in parallel. The component R_g, $R_{gb}\|Q$ represents the ionic conductivity through the grain and GB, respectively.[57]

The total resistance is calculated by using the equation:[58]

$$R_t = R_g + R_{gb} \quad (2)$$

where R_g and R_{gb} are the grain and GB resistance, respectively.

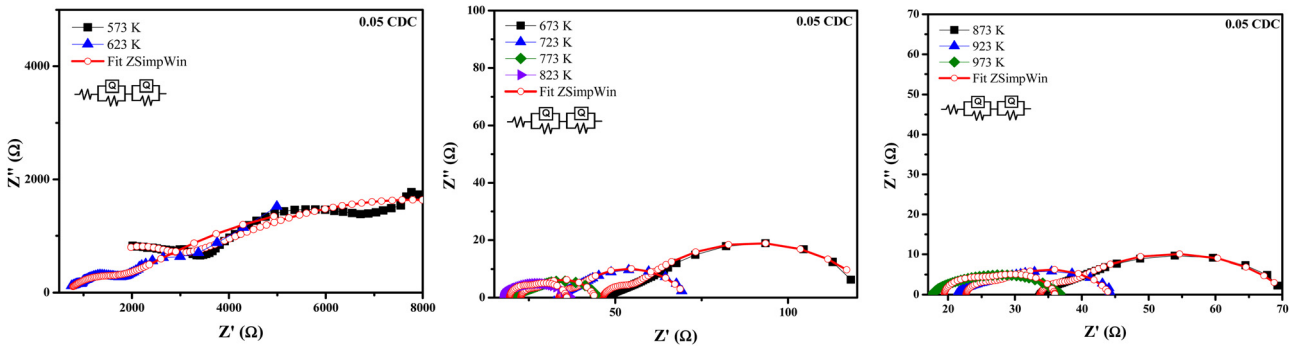

Fig. 9 Nyquist plots of 0.05 CDC measured at temperatures between 573–973 K.

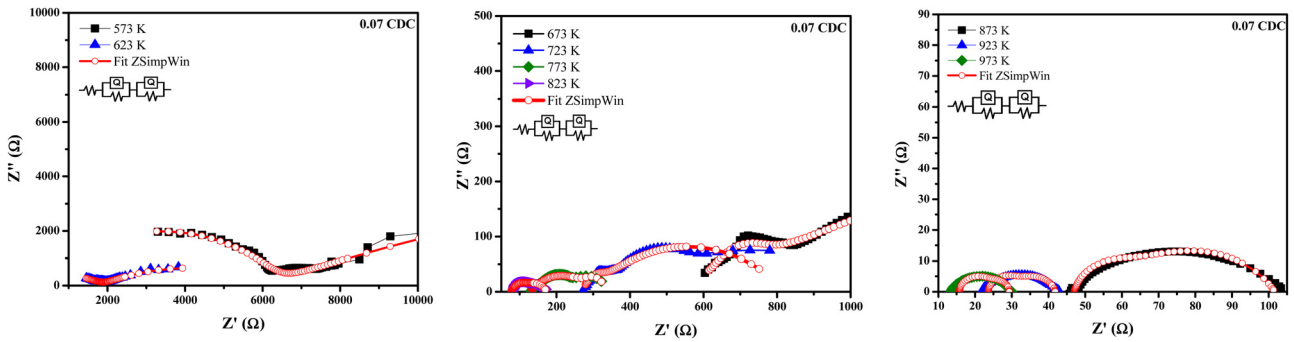

Fig. 10 Nyquist plots of 0.07 CDC measured between temperatures between 573–973 K.

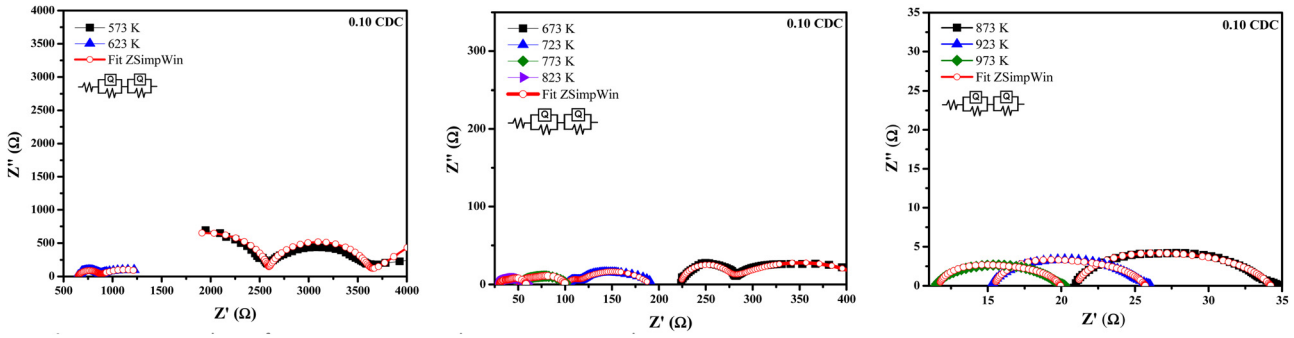

Fig. 11 Nyquist plots of 0.07 CDC measured at temperatures between 573–973 K.

Table 2 The EIS fitted data of the 0.03 CDC at different temperatures, 773–973 K

Temp. (K)	R_g (Ω)	R_{gb} (Ω)	R_e (Ω)	Chi-squared
773	67 760	37 810	1247	1.207×10^{-1}
823	6884	10 720	667.5	9.354×10^{-4}
873	5546	1440.0	383.1	3.241×10^{-3}
923	1577	371.40	233.5	1.276×10^{-3}
973	439.9	171.30	157.8	1.285×10^{-3}

Table 3 The EIS fitted data of the 0.05 CDC at different temperatures, 573–973 K

Temp. (K)	R_g (Ω)	R_{gb} (Ω)	R_e (Ω)	Chi-squared
573	11 200	1309	915.0	1.043×10^{-3}
623	10 460	983.3	653.5	6.416×10^{-4}
673	160.9	488.2	297.6	7.340×10^{-4}
723	146.2	327.9	275.1	3.292×10^{-4}
773	59.28	278.8	91.77	1.069×10^{-3}
823	7.242	72.77	46.26	6.226×10^{-3}
873	3.518	33.53	33.73	1.398×10^{-2}
923	17.59	3.943	22.67	3.286×10^{-2}
973	10.66	5.888	19.44	4.480×10^{-2}

Table 4 The EIS fitted data of the 0.07 CDC at different temperatures, 573–973 K

Temp. (K)	R_g (Ω)	R_{gb} (Ω)	Q–n (n)	Chi-squared
573	3229	5796	0.7399	7.710×10^{-4}
623	1823	4664	0.3423	2.662×10^{-4}
673	69.21	2981	0.2269	1.705×10^{-4}
723	537.5	26.02	1	6.719×10^{-4}
773	164.9	45.55	0.8398	4.398×10^{-3}
823	58.45	38.01	0.6798	1.498×10^{-3}
873	41.38	13.36	0.9396	6.413×10^{-3}
923	7.665	10.57	0.7859	3.286×10^{-2}
973	7.734	10.49	0.8609	2.675×10^{-2}

Impedance analysis revealed that the grain and GB conductivity are a function of the temperature rise for all CDC samples. The high and intermediate frequency ranges of the CDC samples for the grain and GB contributions exhibited a rapid ion migration process. The impedance data obtained from the ZSimpWin software confirmed the ionic conduction in all CDC

Table 5 The EIS fitted data of the 0.10 CDC at different temperatures, 573–973 K

Temp. (K)	R_g (Ω)	R_{gb} (Ω)	R_e (Ω)	Chi-squared
573	1354	2528	778.8	1.332×10^{-3}
623	541.3	209.4	647.0	1.412×10^{-4}
673	47.24	164.3	221.9	7.690×10^{-5}
723	80.73	8.665	102.0	8.563×10^{-4}
773	36.17	13.02	51.57	4.881×10^{-3}
823	7.804	20.51	30.29	1.878×10^{-2}
873	8.115	11.46	19.01	4.648×10^{-2}
923	8.461	5.119	15.77	6.557×10^{-2}
973	5.611	1.23	13.33	1.220×10^{-1}

Table 6 Total oxide ion conductivity for the CDC samples

	Conductivity, σ_t (S cm^{-1})			
Temp. (K)	0.03 CDC	0.05 CDC	0.07 CDC	0.10 CDC
573	—	7.62×10^{-6}	1.34×10^{-6}	1.41×10^{-5}
623	—	8.33×10^{-6}	7.91×10^{-6}	7.29×10^{-5}
673	3.84×10^{-8}	1.46×10^{-4}	1.68×10^{-5}	2.58×10^{-4}
723	1.88×10^{-7}	1.50×10^{-4}	9.10×10^{-5}	6.12×10^{-4}
773	9.64×10^{-7}	2.81×10^{-4}	2.43×10^{-4}	1.11×10^{-3}
823	5.78×10^{-6}	1.11×10^{-3}	5.31×10^{-4}	1.92×10^{-3}
873	1.45×10^{-5}	2.57×10^{-3}	9.36×10^{-4}	2.79×10^{-3}
923	5.22×10^{-5}	3.38×10^{-3}	2.81×10^{-3}	4.03×10^{-3}
973	1.66×10^{-4}	4.42×10^{-3}	5.76×10^{-3}	8.01×10^{-3}

solid solutions. The oxygen ion vacancies on the surface of the CDC are responsible for the ionic conduction. The lower grain resistance (R_g) values at higher temperatures show that all CDC samples have better ionic conductivity.[16] The impedance parameters of all CDC samples extracted using the ZSimpWin software are shown in Tables 2–5. The total oxide ion conductivity is estimated by utilizing eqn (1) and is shown in Table 6. The obtained capacitance values in the range of 10^{-12}–10^{-8} F indicated the grain and GB conduction process.[59–61]

The effect of temperature on the oxide ion conductivity was determined by using the Arrhenius relation.

$$\sigma T = A_o \exp\left(\frac{-E_a}{KT}\right) \quad (3)$$

where σ, A_o, T, E_a, and K are the conductivity, pre-exponential constant, temperature, activation energy, and Boltzmann

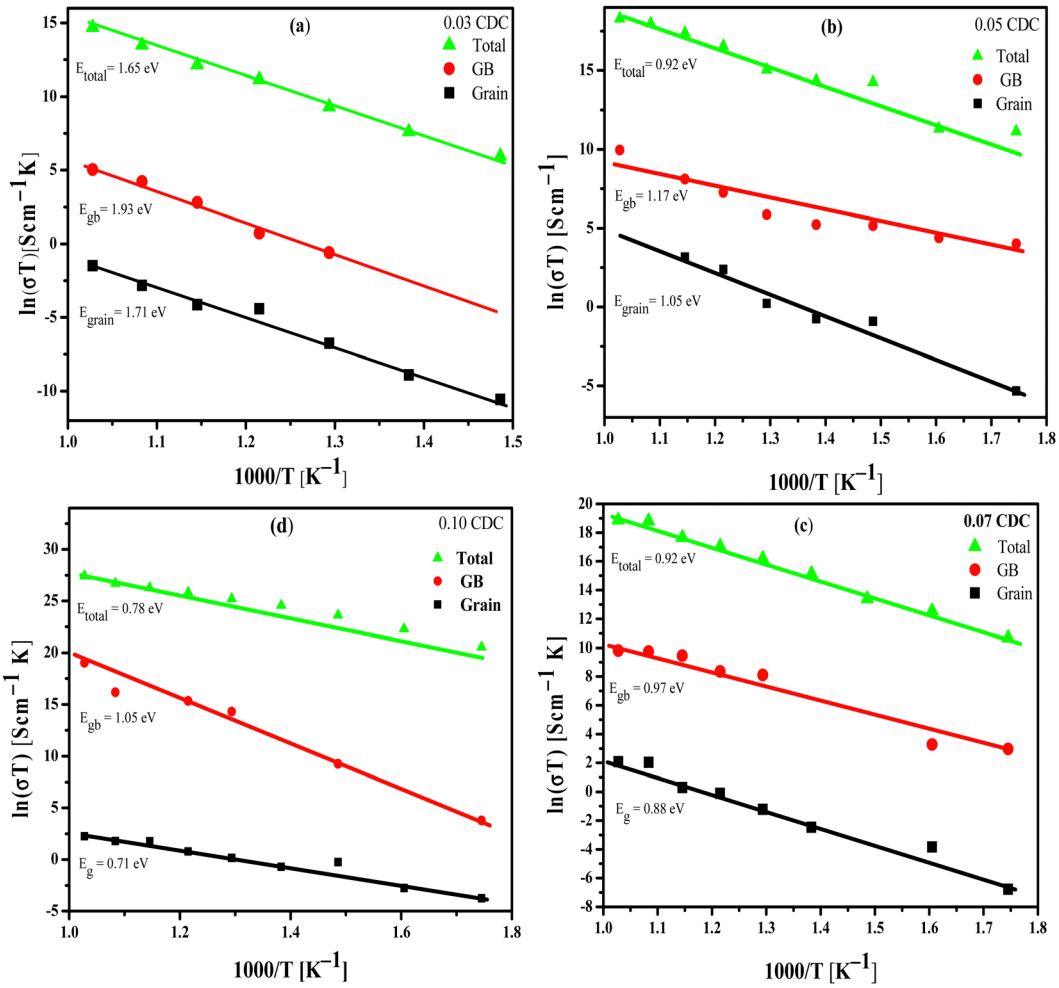

Fig. 12 Arrhenius plots of the total, grain boundary and grain conductivity for (a) 0.03 CDC, (b) 0.05 CDC, (c) 0.07 CDC and (d) 0.10 CDC.

constant, respectively. The Arrhenius plots of the total, grain and GB conductivity of the CDC samples are shown in Fig. 12, and the determined activation energies are shown in Table 7. It has been observed that the activation energy decreases with a rise in the dopant content. The grain conductivity contribution is a major factor for the total oxide ion conductivity in all CDC samples.[62] Thus, the amount of calcium doping affects the conductivity of the ceria. With the ascent in the dopant (Ca) content, a huge expansion in the grain conductivity was seen because of the improvement of the charge transporters emerging from the creation of oxygen vacancies as a result of doping. Hence, this prompted the expansion of the crystal structure.

Table 7 The activation energy of the CDC between the temperatures, 573–973 K

	Activation energy, E_a (eV)		
Sample	Grain	GB	Total
0.03 CDC	1.17	1.93	1.65
0.05 CDC	1.05	1.17	1.01
0.07 CDC	0.88	0.97	0.92
0.10 CDC	0.71	1.05	0.78

The rearranged anion opening at the surface and connection with the electrode assumes a significant part in the improvement of the oxide ion conductivity. The change in the surface oxygen vacancies fundamentally adjusts the physical and chemical properties of the materials. The insertion of the Ca^{2+} dopant into the cerium lattice generates the negatively charged defect, and hence increases the anion vacancies. The effect of the Ca^{2+} doping in CeO_2 is depicted by using Kröger–Vink notation as shown in eqn (4).

$$CaO \xrightarrow{CeO_2} Ca''_{Ce} + O_o + V_o^{\bullet\bullet} \quad (4)$$

At elevated temperature, the surplus electrons and anion vacancies are in equilibrium with the gas phase, as shown in eqn (5).[63] The surplus electrons may arise due to small Ce^{3+} polarons, which is in corroboration with the obtained XPS data and small conduction bandwidth.

$$O_o \rightleftarrows V_o^{\bullet\bullet} + 2e' + \frac{1}{2}O_{2(g)} \quad (5)$$

Thus, the improved mobility for the oxygen ions could lead to the high oxide ion conductivity for the CDC samples.[64] Since calcium has likewise been viewed as a sintering aid for the

ceria-based electrolytes, in this way it helps to achieve the high densification at a lower sintering temperature.[65,66] Subsequently, with the ascent in the Ca content, the augmentation in the relative densities of these CDC samples has been clearly observed, as displayed in Table 1. The high densification of the CDC samples could facilitate the versatility of charge transporters at GB, and consequently it assists with improvement on the conductivity of the CDC. From the obtained results, it has been seen that the high oxide conductivities of 1.66×10^{-4}, 4.42×10^{-3}, 5.76×10^{-3}, and 8.01×10^{-3} S cm^{-1} were recorded at 973 K with lower activation energies (E_a) of 1.65, 1.01, 0.92 and 0.78 eV for the 0.03 CDC, 0.05 CDC, 0.07 CDC, and 0.10 CDC, respectively.

The conductivity improves as a function of the dopant concentration. The 0.10 CDC shows the most noteworthy conductivity in the order of 8.01×10^{-3} S cm^{-1} at 973 K with a lower E_a of 0.78 eV, among all CDC samples studied here. The obtained conductivity values for the CDC were viewed as competent when contrasted with the ionic conductivity of 7.7×10^{-2} S cm^{-1} of $Ce_{0.8}Sm_{0.2}O_{2-\delta}$,[67] 3.6×10^{-2} S cm^{-1} of $Ce_{0.9}Gd_{0.1}O_{2-\delta}$,[68] 8.89×10^{-3} S cm^{-1} of $Ce_{0.9}La_{0.1}O_{2-\delta}$[69] at 973 K, 5.9×10^{-3} S cm^{-1} of $Ce_{0.9}La_{0.1}O_{2-\delta}$[70] and 9.4×10^{-4} S cm^{-1} of $Ce_{0.85}La_{0.15}O_{2-\delta}$ at 873 K[71] like potential electrolyte materials of IT – SOFCs. The obtained conductivity for 0.10 CDC in the order of 8.01×10^{-3} S cm^{-1} at 973 K with E_a of 0.78 eV can likewise be contrasted best with the conductivities of $Ce_{0.9}Ca_{0.1}O_{2-\delta}$ (8.02×10^{-3}, 6.31×10^{-3}, 1.13×10^{-3} S cm^{-1} at 973 K with activation energies of 0.84, 0.86 and 0.89 eV) sample, synthesized from the combustion route using citric acid, glycine, and urea as a fuel, as reported by Ong *et al.*[72] The high grain conductivity of the prepared CDC may be connected with the lower confinement of the dopant (Ca) at the GB.

Along these lines, bringing down the comparison space charge impacts could bring about a huge augmentation of oxide ion conductivity. In the current work, the 0.05, 0.07, and 0.10 CDC synthesized from the facile solid-state route showed the ionic conductivity in the order of 10^{-3} S cm^{-1} at 973 K. The lower E_a obtained for 0.1 CDC (0.78 eV) is nearly identical to the oxide ion conductivity of $Ce_{0.9}Ca_{0.1}O_{1.9}$ synthesized from the auto – combustion route with citric acid, glycine and urea as fuels, as reported by Ong *et al.*[58] Thus, the substantially more affordable Ca-doped ceria (CDC) materials have showed significant outcomes in contrast to those more costly rare-earth doped ceria-based materials, and could assist with decreasing the expense for SOFCs. Consequently, Ca-doped ceria-based ceramics could be viewed as potential electrolyte materials for IT-SOFC applications.

Conclusion

The Ca-doped ceria (CDC) samples having composition $Ce_{(1-x)}Ca_xO_{2-\delta}$ [x = 0.03–0.1] were successfully prepared by using a cost-effective and conventional solid – state method. All CDC were sintered at lower temperature of 1473 K than required. The XRD, Raman, XPS, and FESEM – EDX analysis confirmed the formation of the single-phase solid solution of these CDC. The 0.10 CDC showed an essentially upgraded oxide ion conductivity in the order of 8.01×10^{-3} S cm^{-1} at 973 K with a lower activation energy, E_a = 0.78 eV, in contrast to the other CDC. The critical improvement in the physical and electrochemical properties of the CDC through solid – state synthesis has been accomplished. Thus, monetarily reasonable CDC samples might be viewed as a potential electrolyte material for IT-SOFC applications.

Author contributions

Dr Naeemakhtar Momin: investigation, conceptualization, writing – original draft preparation, Prof. J. Manjanna: supervision, writing – review & editing, Prof. Satoru Kobayashi: resources, visualization, Dr Aruna S. T.: project administration, supervision, Dr Senthil Kumar S: formal analysis, validation, Dr G.P. Nayaka: resource.

Conflicts of interest

The authors declare that they have no known competing financial interests or personal relationships that could have appeared to influence the work reported in this paper.

Acknowledgements

The authors greatly acknowledge the financial support from (i) VGST-CESEM, GRD – 746, Ministry of IT, BT and S & T, Govt. of Karnataka; (ii) DST-FIST, Govt. of India [SR/FST/CSI-273/2016]; and (iii) Rani Channamma University, Belagavi – Interdisciplinary Research Project, 2022-23.

References

1 J. B. Goodenough, Oxide-ion electrolytes, *Annu. Rev. Mater. Res.*, 2003, **33**, 91, DOI: 10.1146/annurev.matsci.33.022802.091651.
2 M. Mogensen, Physical, chemical and electrochemical properties of pure and doped ceria, *Solid State Ionics*, 2000, **129**, 63, DOI: 10.1016/S0167-2738(99)00318-5.
3 T. Ahmad, M. Shahazad, M. Ubaidullah, J. Ahmed, A. Khan and A. M. El-Toni, Structural characterization and dielectric properties of ceria-titania nanocomposites in low ceria region, *Mater. Res. Express*, 2017, **4**, 125016, DOI: 10.1088/2053-1591/aa9c51.
4 T. Zhang, J. Ma, L. Kong, S. Chan and J. Kilner, Aging behavior and ionic conductivity of ceria-based ceramics: A comparative study, *Solid State Ionics*, 2004, **170**, 209, DOI: 10.1016/j.ssi.2004.03.003.
5 K. Eguchi, T. Setoguchi, T. Inoue and H. Arai, Electrical properties of ceria-based oxides and their application to solid oxide fuel cells, *Solid State Ionics*, 1992, **52**, 165, DOI: 10.1016/0167-2738(92)90102-U.
6 Y. Zheng, H. Gu, H. Chen, L. Gao, X. Zhu and L. Guo, Effect of Sm and Mg co-doping on the properties of ceria-based

electrolyte materials for IT-SOFCs, *Mater. Res. Bull.*, 2009, **44**, 775, DOI: 10.1016/j.materresbull.2008.09.021.

7 K. Yamashita, K. V. Ramanujachary and M. Greenblatt, Hydrothermal synthesis and low temperature conduction properties of substituted ceria ceramics, *Solid State Ionics*, 1995, **81**, 53, DOI: 10.1016/0167-2738(95)99031-H.

8 S. Banerjee and P. S. Devi, Understanding the effect of calcium on the properties of ceria prepared by a mixed fuel process, *Solid State Ionics*, 2008, **179**, 661, DOI: 10.1016/j.ssi.2008.04.008.

9 H. Yahiro, T. ohuchi, K. Eguchi and H. Arai, Electrical properties and microstructure in the system ceria-alkaline earth oxide, *J. Mater. Sci.*, 1988, **23**, 1036, DOI: 10.1007/BF01154008.

10 Y. Ma, X. Wang, H. A. Khalifa, B. Zhu and M. Muhammed, Enhanced ionic conductivity in calcium doped ceria – carbonate electrolyte: A composite effect, *Int. J. Hydrogen Energy*, 2012, **37**, 19401, DOI: 10.1016/j.ijhydene.2011.09.122.

11 Y. Lin, S. Fang, D. Su, K. S. Brinkman and F. Chen, Enhancing grain boundary ionic conductivity in mixed ionic–electronic conductors, *Nat. Commun.*, 2015, **6**, 6824, DOI: 10.1038/ncomms7824.

12 J. Garcia-Barriocanal, A. Rivera-Calzada, M. Varela, Z. Sefrioui, E. Iborra, C. Leon, S. J. Pennycook and J. Santamaria, Colossal ionic conductivity at interfaces of epitaxial ZrO_2:Y_2O_3/$SrTiO_3$ heterostructures, *Science*, 2008, **321**, 676, DOI: 10.1126/science.1156393.

13 B. Wang, Y. Cai, C. Xia, J.-S. Kim, Y. Liu, W. Dong, H. Wang, M. Afzal, J. Li, R. Raza and B. Zhu, Semiconductor-ionic membrane of LaSrCoFe-oxide-doped ceria solid oxide fuel cells, *Electrochim. Acta*, 2017, **248**, 496, DOI: 10.1016/j.electacta.2017.07.128.

14 Y. Lu, J. Li, L. Ma, Z. Lu, L. Yu and Y. Cai, The development of semiconductor-ionic conductor composite electrolytes for fuel cells with symmetrical electrodes, *Int. J. Hydrogen Energy*, 2021, **46**, 9835, DOI: 10.1016/j.ijhydene.2020.05.240.

15 Y. Lu, M. Akbar, J. Li, L. Ma, B. Wang and C. Xia, A p–n–n heterostructure composite for low-temperature solid oxide fuel cells, *J. Alloys Compd.*, 2022, **890**, 161765, DOI: 10.1016/j.jallcom.2021.161765.

16 M. A. K. Y. Shah, N. Mushtaq, S. Rauf, N. Akbar, Y. Xing, Y. Wu, B. Wang and B. Zhu, Advanced fuel cell based on semiconductor perovskite La–$BaZrYO_{3-\delta}$ as an electrolyte material operating at low temperature 550 °C, *Int. J. Hydrogen Energy*, 2020, **45**, 27501, DOI: 10.1016/j.ijhydene.2020.07.011.

17 L. Li, Q. Shi, L. Huang, C. Yan and Y. Wu, Green synthesis of faujasite-$La_{0.6}Sr_{0.4}Co_{0.2}Fe_{0.8}O_{3-\delta}$ mineral nanocomposite membrane for low temperature advanced fuel cells, *Int. J. Hydrogen Energy*, 2021, **46**, 9826, DOI: 10.1016/j.ijhydene.2020.05.275.

18 N. Akbar, S. Paydar and Y. Wu, Tuning an ionic-electronic mixed conductor $NdBa_{0.5}Sr_{0.5}Co_{1.5}Fe_{0.5}O_{5+\delta}$ for electrolyte functions of advanced fuel cells, *Int. J. Hydrogen Energy*, 2021, **46**, 9847, DOI: 10.1016/j.ijhydene.2020.05.220.

19 S. Paydar, N. Akbar, Q. Shi and Y. Wu, Developing cuprospinel $CuFe_2O_4$–ZnO semiconductor heterostructure as a proton conducting electrolyte for advanced fuel cells, *Int. J. Hydrogen Energy*, 2021, 9927, DOI: 10.1016/j.ijhydene.2020.04.198.

20 X. Chen, B. Dong, Q. A. Islam, H. Song and Y. Wu, Semiconductor-ionic properties and device performance of heterogeneous La-doped CeO_2–ZnO nanocomposites, *Int. J. Hydrogen Energy*, 2021, **46**, 9968, DOI: 10.1016/j.ijhydene.2020.04.174.

21 Q. Shi, J. Chen, Y. Xing, B. Zhu and Y. Wu, Semiconductor heterostructure $SrTiO_3$/CeO_2 electrolyte membrane fuel cells, *J. Electrochem. Soc.*, 2020, **167**, 054504, DOI: 10.1149/2.0082005jes.

22 Y. Xing, Y. Wu, L. Li, Q. Shi, J. Shi, S. Yun, M. Akbar, B. Wang, J. S. Kim and B. Zhu, Proton shuttles in CeO_2/$CeO_{2-\delta}$ core–shell structure, *ACS Energy Lett.*, 2019, **4**, 2601, DOI: 10.1021/acsenergylett.9b01829.

23 K. Yamashita, K. V. Ramanujachary and M. Greenblatt, Hydrothermal synthesis and low temperature conduction properties of substituted ceria ceramics, *Solid State Ionics*, 1995, **81**, 53, DOI: 10.1016/0167-2738(95)99031-H.

24 Y. Dong, S. Hampshire, B. Lin, Y. Ling and X. Zhang, High sintering activity Cu–Gd co-doped CeO_2 electrolyte for solid oxide fuel cells, *J. Power Sources*, 2010, **195**, 6510, DOI: 10.1016/j.jpowsour.2010.03.053.

25 B. Zhu, X. Liu, M. Sun, S. Ji and J. Sun, Calcium doped ceria-based materials for cost-effective intermediate temperature solid oxide fuel cells, *Solid State Sci.*, 2003, **5**, 1127, DOI: 10.1016/S1293-2558(03)00123-7.

26 T. S. Zhang, J. Ma, H. T. Huang, P. Hing, Z. T. Xia, S. H. Chan and J. A. Kilner, Effects of dopant concentration and aging on the electrical properties of Y-doped ceria electrolytes, *Solid State Sci.*, 2003, **5**, 1505, DOI: 10.1016/j.solidstatesciences.2003.10.001.

27 M. G. Chourashiya and L. D. Jadhav, synthesis and characterization of 10% Gd doped ceria (GDC) deposited on NiO-GDC anode-grade-ceramic substrate as half cell for IT-SOFC, *Int. J. Hydrogen Energy*, 2011, **36**, 14984, DOI: 10.1016/j.ijhydene.2010.12.083.

28 B. Feng, I. Sugiyama, H. Hojo, H. Ohta, N. Shibata and Y. Ikuhara, Atomic structures and oxygen dynamics of CeO_2 grain boundaries, *Sci. Rep.*, 2016, **6**, 20288, DOI: 10.1038/srep20288.

29 W. H. Weber, K. C. Hass and J. R. McBride, Raman study of CeO_2: Second-order scattering, lattice dynamics, and particle-size effects, *Phys. Rev. B: Condens. Matter Mater. Phys.*, 1993, **48**, 178, DOI: 10.1103/PhysRevB.48.178.

30 X. Liu, S. Chen and X. Wang, Synthesis and photoluminescence of CeO_2:Eu^{3+} phosphor powders, *J. Lumin.*, 2007, **127**, 650, DOI: 10.1016/j.jlumin.2007.03.014.

31 S. Patil, S. Seal, Y. Guo, A. Schulte and J. Norwood, Role of trivalent La and Nd dopants in lattice distortion and oxygen vacancy generation in cerium oxide nanoparticles, *Appl. Phys. Lett.*, 2006, **88**, 243110, DOI: 10.1063/1.2210795.

32 M. Kurian and C. Kunjachan, Investigation of size dependency on lattice strain of nanoceria particles synthesised by wet chemical methods, *Int. Nano Lett.*, 2014, **4**, 73, DOI: 10.1007/s40089-014-0122-7.

33 T. Ahmad and A. K. Ganguli, Reverse micellar route to nanocrystalline titanates ($SrTiO_3$, Sr_2TiO_4, and $PbTiO_3$): Structural aspects and dielectric properties, *J. Am. Ceram. Soc.*, 2006, **89**, 1326, DOI: 10.1111/j.1551-2916.2005.00886.x.

34 R. Tholkappiyan and K. Vishista, Combustion synthesis of Mg–Er ferrite nanoparticles: Cation distribution and structural, optical, and magnetic properties, *Mater. Sci. Semicond. Process.*, 2015, **40**, 631, DOI: 10.1016/j.mssp.2015.06.076.

35 A. K. Tripathi, M. C. Mathpal, P. Kumar, M. K. Singh, M. A. G. Soler and A. Agarwal, Structural, optical and photoconductivity of Sn and Mn doped TiO_2 nanoparticles, *J. Alloys Compd.*, 2015, **622**, 37, DOI: 10.1016/j.jallcom.2014.09.218.

36 M. Zawadzki, Preparation and characterization of ceria nanoparticles by microwave-assisted solvothermal process, *J. Alloys Compd.*, 2008, **454**, 347, DOI: 10.1016/j.jallcom.2006.12.078.

37 T. Suzuki, I. Kosacki, H. U. Anderson and P. Colomban, Electrical conductivity and lattice defects in nanocrystalline cerium oxide thin films, *J. Am. Ceram. Soc.*, 2004, **84**, 2007, DOI: 10.1111/j.1151-2916.2001.tb00950.x.

38 R. Kostić, S. Aškrabić, Z. Dohčević-Mitrović and Z. V. Popović, Low-frequency Raman scattering from CeO_2 nanoparticles, *Appl. Phys. A: Mater. Sci. Process.*, 2008, **90**, 679, DOI: 10.1007/s00339-007-4345-6.

39 J. E. Spanier, R. D. Robinson, F. Zhang, S.-W. Chan and I. P. Herman, Size-dependent properties of CeO_{2-y} nanoparticles as studied by Raman scattering, *Phys. Rev. B: Condens. Matter Mater. Phys.*, 2001, **64**, 245407, DOI: 10.1103/PhysRevB.64.245407.

40 W. F. Zhang, Y. L. He, M. S. Zhang, Z. Yin and Q. Chen, Raman scattering study on anatase TiO_2 nanocrystals, *J. Phys. D: Appl. Phys.*, 2000, **33**, 912, DOI: 10.1088/0022-3727/33/8/305.

41 H. C. Choi, Y. M. Jung and S. Bin Kim, Size effects in the Raman spectra of TiO_2 nanoparticles, *Vib. Spectrosc.*, 2005, **37**, 33, DOI: 10.1016/j.vibspec.2004.05.006.

42 V. V. Pushkarev, V. I. Kovalchuk and J. L. D'Itri, Probing defect sites on the CeO_2 surface with dioxygen, *J. Phys. Chem. B*, 2004, **108**, 5341, DOI: 10.1021/jp0311254.

43 X. Garcia, L. Soler, N. J. Divins, X. Vendrell, I. Serrano, I. Lucentini, J. Prat, E. Solano, M. Tallarida, C. Escudero and J. Llorca, Ceria-based catalysts studied by near ambient pressure x-ray photoelectron spectroscopy: A review, *Catalysts*, 2020, **10**, 286, DOI: 10.3390/catal10030286.

44 M. A. M. Khan, W. Khan, M. Ahamed and A. N. Alhazaa, Microstructural properties and enhanced photocatalytic performance of Zn doped CeO_2 nanocrystals, *Sci. Rep.*, 2017, **7**, 1, DOI: 10.1038/s41598-017-11074-7.

45 S. A. Acharya, V. M. Gaikwad, S. W. D'Souza and S. R. Barman, Gd/Sm dopant-modified oxidation state and defect generation in nano-ceria, *Solid State Ionics*, 2014, **260**, 21, DOI: 10.1016/j.ssi.2014.03.008.

46 P. Datta, P. Majewski and F. Aldinger, Study of gadolinia-doped ceria solid electrolyte surface by XPS, *Mater. Charact.*, 2009, **60**, 138–143, DOI: 10.1016/j.matchar.2008.08.002.

47 X. L. Zhao, J. J. Liu, T. Xiao, J. C. Wang, Y. X. Zhang, H. C. Yao, J. S. Wang and Z. J. Li, Effect of Ca co-dopant on the electrical conductivity of Gd-doped ceria, *J. Electroceram.*, 2012, **28**, 149, DOI: 10.1007/s10832-012-9696-5.

48 M. Yan, T. Mori, J. Zou, F. Ye, D. R. Ou and J. Drennan, TEM and XPS analysis of $Ca_xCe_{1-x}O_{2-y}$ (x = 0.05–0.5) as electrolyte materials for solid oxide fuel cells, *Acta Mater.*, 2009, **57**, 722–731, DOI: 10.1016/j.actamat.2008.10.014.

49 J. L. M. Rupp, T. Drobek, A. Rossi and L. J. Gauckler, Chemical analysis of spray pyrolysis gadolinia-doped ceria electrolyte thin films for solid oxide fuel cells, *Chem. Mater.*, 2007, **19**, 1134, DOI: 10.1021/cm061449f.

50 A. Kossoy, H. Cohen, T. Bendikov, E. Wachtel and I. Lubomirsky, Water adsorption at the surface of pure and Gd-doped ceria, *Solid State Ionics*, 2011, **194**, 1–4, DOI: 10.1016/j.ssi.2011.05.011.

51 S. A. Acharya, V. M. Gaikwad, S. W. D'Souza and S. R. Barman, Gd/Sm dopant-modified oxidation state and defect generation in nano-ceria, *Solid State Ionics*, 2014, **260**, 21, DOI: 10.1016/j.ssi.2014.03.008.

52 P. Datta, P. Majewski and F. Aldinger, Study of gadolinia-doped ceria solid electrolyte surface by XPS, *Mater. Charact.*, 2009, **60**, 138, DOI: 10.1016/j.matchar.2008.08.002.

53 D. Manoharan and K. Vishista, Optical Properties of Nanocrystalline cerium dioxide synthesized by single step aqueous citrate-nitrate gel combustion method, *Asian J. Chem.*, 2013, **25**, 9045, DOI: 10.14233/ajchem.2013.14984.

54 K. Amarsingh Bhabu, J. Theerthagiri, J. Madhavan, T. Balu, G. Muralidharan and T. R. Rajasekaran, Cubic fluorite phase of samarium doped cerium oxide $(CeO_2)_{0.96}Sm_{0.04}$ for solid oxide fuel cell electrolyte, *J. Mater. Sci.: Mater. Electron.*, 2016, **27**, 1566, DOI: 10.1007/s10854-015-3925-z.

55 V. Thangadurai and P. Kopp, Chemical synthesis of Ca-doped CeO_2 intermediate temperature oxide ion electrolytes, *J. Power Sources*, 2007, **168**, 178, DOI: 10.1016/j.jpowsour.2007.03.030.

56 P. Venkataswamy, D. Jampaiah, A. E. Kandjani, Y. M. Sabri, B. M. Reddy and M. Vithal, Transition (Mn, Fe) and rare earth (La, Pr) metal doped ceria solid solutions for high performance photocatalysis: Effect of metal doping on catalytic activity, *Res. Chem. Intermed.*, 2018, **44**, 2523, DOI: 10.1007/s11164-017-3244-5.

57 A. Ali, R. Raza, M. Kaleem Ullah, A. Rafique, B. Wang and B. Zhu, Alkaline earth metal and samarium co-doped ceria as efficient electrolytes, *Appl. Phys. Lett.*, 2018, **112**, 043902, DOI: 10.1063/1.5005824.

58 K. C. Anjaneya, G. P. Nayaka, J. Manjanna, G. Govindaraj and K. N. Ganesha, Preparation and characterization of $Ce_{1-x}Gd_xO_{2-\delta}$ (x = 0.1–0.3) as solid electrolyte for intermediate temperature SOFC, *J. Alloys Compd.*, 2013, **578**, 53, DOI: 10.1016/j.jallcom.2013.05.010.

59 M. V. Ganduglia-Pirovano, A. Hofmann and J. Sauer, Oxygen vacancies in transition metal and rare earth oxides: Current state of understanding and remaining challenges, *Surf. Sci. Rep.*, 2007, **62**, 219, DOI: 10.1016/j.surfrep.2007.03.002.

60 M. F. García-sánchez, J. M. Peko, A. R. Ruiz-salvador, G. Rodríguez-gattorno and Y. Echevarría, An elementary picture

of dielectric spectroscopy in solids: Physical basis, *J. Chem. Educ.*, 2003, **80**, 1062–1063, DOI: 10.1021/ed080p1062.

61 N. Momin, J. Manjanna, K. S. Rane, A. Kumar, S. Senthilkumar and S. T. Aruna, Structural and ionic conductivity of Cu-doped titania ($Ti_{0.95}Cu_{0.05}O_{2-\delta}$) for high temperature energy devices, *Ceram. Int.*, 2021, **47**, 10284, DOI: 10.1016/j.ceramint.2020.06.277.

62 K. Zhao and Y. Du, Calcium-doped ceria materials for anode of solid oxide fuel cells running on methane fuel, *J. Power Sources*, 2017, **347**, 79, DOI: 10.1016/j.jpowsour.2017.01.113.

63 J. Maier, Electronic transport in single crystals of Gd-doped ceria, *J. Electrochem. Soc.*, 2007, **156**, 583–587, DOI: 10.1149/1.2722530.

64 H. Song and U. S. Ozkan, Changing the oxygen mobility in Co/ceria catalysts by ca incorporation: Implications for ethanol steam reforming, *J. Phys. Chem. A*, 2010, **114**, 3796, DOI: 10.1021/jp905608e.

65 S. Banerjee, P. S. Devi, D. Topwal, S. Mandal and K. Menon, Enhanced ionic conductivity in $Ce_{0.8}Sm_{0.2}O_{1.9}$ unique effect of calcium co-doping, *Adv. Funct. Mater.*, 2007, **17**, 2847, DOI: 10.1002/adfm.200600890.

66 N. Momin and J. Manjanna, Ionic conductivity of $Ce_{0.91}Ca_{0.09}O_{2-\delta}$ as an electrolyte for intermediate temperature solid oxide fuel cells, *Res. J. Chem. Environ.*, 2021, **25**(12), DOI: 10.25303/2512rjce001009.

67 N. Jaiswal, D. Kumar, S. Upadhyay and O. Parkash, Ceria co-doped with calcium (Ca) and strontium (Sr): A potential candidate as a solid electrolyte for intermediate temperature solid oxide fuel cells, *Ionics*, 2014, **20**, 45, DOI: 10.1007/s11581-013-0936-8.

68 A. Z. Liu, J. X. Wang, C. R. He, H. Miao, Y. Zhang and W. G. Wang, Synthesis and characterization of $Gd_{0.1}Ce_{0.9}O_{1.95}$ nanopowder *via* an acetic-acrylicmethod, *Ceram. Int.*, 2013, **39**, 6229, DOI: 10.1016/j.ceramint.2013.01.044.

69 N. Momin, J. Manjanna, L. D'Souza, S. T. Aruna and S. Senthil Kumar, Synthesis, structure and ionic conductivity of nanocrystalline $Ce_{1-x}La_xO_{2-\delta}$ as an electrolyte for intermediate temperature solid oxide fuel cells, *J. Alloys Compd.*, 2022, **896**, 163012, DOI: 10.1016/j.jallcom.2021.163012.

70 S. Dikmen, P. Shuk and M. Greenblatt, Hydrothermal synthesis and properties of $Ce_{1-x}La_xO_{2-\delta}$ solid solutions, *Solid State Ionics*, 1999, **126**, 89, DOI: 10.1016/S0167-2738(99)00146-0.

71 N. Jaiswal, S. Upadhyay, D. Kumar and O. Parkash, Ionic conductivity investigation in lanthanum (La) and strontium (Sr) co-doped ceria system, *J. Power Sources*, 2013, **222**, 230, DOI: 10.1016/j.jpowsour.2012.08.095.

72 P. S. Ong, Y. P. Tan, Y. H. Taufiq-Yap and Z. Zainal, Improved sinterability and conductivity enhancement of 10 mol% calcium-doped ceria using different fuel-aided combustion reactions and its structural characterisation, *Mater. Sci. Eng., B*, 2014, **185**, 26, DOI: 10.1016/j.mseb.2014.01.016.